

Characteristics of Radiating Collapse at the Density Limit in the Large Helical Device

Byron J. PETERSON, Junichi MIYAZAWA, Kiyohiko NISHIMURA, Suguru MASUZAKI, Yoshio NAGAYAMA, Nobuyoshi OHYABU, Hiroshi YAMADA, Kozo YAMAZAKI, Takako KATO, Izumi MURAKAMI, Naoko ASHIKAWA, Yuhong XU¹⁾, Artem Y. KOSTRIOUKOV²⁾, Yi LIU³⁾, Ryuichi SAKAMOTO, Motoshi GOTO, Kazumichi NARIHARA, Masaki OSAKABE, Kenji TANAKA, Tokihiko TOKUZAWA, Mamoru SHOJI, Hisamichi FUNABA, Shigeru MORITA, Tomohiro MORISAKI, Osamu KANEKO, Kazuo KAWAHATA, Akio KOMORI, Shigeru SUDO, Osamu MOTOJIMA and the LHD Experiment Group

National Institute for Fusion Science, Toki 509-5292 Japan

¹⁾*Forschungszentrum Jülich, Jülich, Germany*

²⁾*St. Petersburg Technical University, St. Petersburg, Russia*

³⁾*Southwest Institute of Physics, Chengdu, China*

(Received 24 January 2006 / Accepted 19 June 2006)

Steady state densities of up to $1.6 \times 10^{20} \text{ m}^{-3}$ have been sustained using gas puff fuelling and NBI heating up to 11 MW in the Large Helical Device (LHD). The density limit in LHD is observed to be greater than 1.6 times the Sudo limit. The density is ultimately limited by a radiating collapse which is attributed to the onset of a radiative thermal instability of the light impurities in the edge region of the plasma based on several recent observations in LHD. First of all the onset of the radiative thermal instability is tied to a certain edge temperature threshold. Secondly, the onset of the thermal instability occurs first in oxygen and then carbon as expected from their cooling rate temperature dependencies. Finally, radiation profiles show that as the temperature drops and the plasma collapses the radiating zone broadens and moves inward. In addition, comparison of impurity lines with the total radiated power behaviour suggests that carbon is the dominant radiator. Two dimensional tomographic inversions of Absolute eXtreme UltraViolet Diode (AXUVD) array data and comparison of modelling with images of radiation brightness from imaging bolometers indicate that the poloidal asymmetry which accompanies the radiating collapse is roughly toroidally symmetric.

© 2006 The Japan Society of Plasma Science and Nuclear Fusion Research

Keywords: Large Helical Device, density limit, radiating collapse, carbon impurity, edge electron temperature, imaging bolometer, poloidal asymmetry

DOI: 10.1585/pfr.1.045

1. Introduction

Density limit is an important issue for future fusion reactors since the fusion reaction rate is a function of the density squared. In tokamaks an empirical density limit (Greenwald limit) has been observed which scales with the plasma current density. Densities above the Greenwald limit have been achieved primarily in tokamaks using pellet injection to achieve peaked density profiles, indicating that the density limiting process is related to the physics of the edge plasmas. As the density limit in a tokamak is approached, the MARFE phenomenon is commonly observed and the discharge is ultimately terminated by a current disruption which can cause considerable damage to the device from induced currents and runaway electrons [1].

On the other hand, the operational density in stellara-

tors is not limited by current disruption as in tokamaks, nor is the Greenwald limit directly applicable to net-current free plasmas. In stellarator devices the density is limited by a radiation induced temperature collapse as was shown by the transport modelling of data from the Advanced Toroidal Facility (ATF) [2]. Studies on Heliotron-E resulted in an empirical density limit scaling law (Sudo limit) which is proportional to the square root of the product of the input power density and the magnetic field [3]. This limit was determined by the scaling of the density reached when the stored energy peaks, which is the point at which the global power balance seems to be lost and the stored energy begins to decrease. This limit does not necessarily represent the true operational density limit as the drop in the stored energy can be attributed in part to the reduced confinement of the high density regime which is discussed in the final paragraph of this section. In ATF mea-

author's e-mail: peterston@LHD.nifs.ac.jp

measurements of radiation profiles using bolometers showed the inward propagation of the radiation zone driving the thermal collapse. This was attributed to a loss of the local power balance at the edge and thought to be triggered by the radiative thermal instability of impurities in the low temperature edge [4]. This hypothesis was further supported by transport modelling of the ATF plasmas which showed that light impurities would radiate primarily from the edge and could result in 30% radiated power fractions at the thermal collapse, whereas heavier impurities would radiate from the core and could result in 100% radiated power fractions at the collapse. The collapse in the former case of light impurities was partly attributed to limitations on the thermal conduction from the core to the edge resulting in the edge localized power imbalance [5]. In the W7-AS stellarator, using a graphite limiter configuration, the density limit was attributed to power imbalance due to strong radiation from heavy impurities from the core of the plasma. This study also revealed a density limit scaling law very similar to the Sudo limit [6]. With the addition of a graphite island divertor in W7-AS, at high densities the radiation profile became hollow with the pumping out of impurities from the core and much higher steady state densities of up to $3.5 \times 10^{20} \text{ m}^{-3}$ could be achieved. However, when the higher deposited power was considered the previously derived scaling law was still obeyed [7].

Initial investigations into the density limit on the Large Helical Device (LHD) [8] have indicated that the density in LHD is limited by a radiative thermal instability which results in the collapse of the plasma at a limit which is greater than 1.4 times the Sudo limit. This collapse is characterized by a poloidal asymmetry in the radiation and density with the high density and high radiation region on the inboard side. In W7-AS a poloidal radiation asymmetry is also observed as the density limit was approached [9]. Further investigation of this phenomenon in LHD showed that the poloidal asymmetry also appears in the electron temperature profiles (lower temperature on the inboard side) as the plasma column contracts [10]. Measurements with imaging bolometers indicated that the radiation asymmetry was located on the inboard side slightly below the midplane [11]. Also, after boronization of the vacuum vessel wall, indeed, the radiation loss, P_{rad} , decreases about 20~50%, compared at similar density and input power, P_{abs} , and the density limit increases 20~50% [12]. These results indicate the importance of P_{rad} on density limit studies. However, the thermal instability is typically triggered even when P_{rad} is less than a half of P_{abs} as in the case of ATF [4, 5]. These observations call for an investigation of the role of P_{rad} and the exploration of the mechanism which triggers or enhances the thermal instability in LHD.

Other than the operational density limit, where the discharge is terminated by radiating collapse, a confinement limit has been recognized in LHD [13–16]. The energy confinement times, τ_E , of the moderated density LHD

plasmas are well reproduced by the international stellarator scaling 1995 (ISS95) [17] with an improvement factor of roughly 1.5. ISS95 has strong positive density dependence as $\tau_E \propto \bar{n}_e^{0.51}$. In the high-density regime, however, the energy confinement is lower than the prediction of ISS95. This confinement limit appears at lower density than the operational density limit, similar to the saturated ohmic confinement in tokamaks [18]. Studies on the confinement limit have been carried out in Refs. [13–16], from the points of view of the shallow heating beam penetration and the parameter dependence of the thermal diffusivity in the high-density regime. In this study, we will focus on the operational density limit, reporting the most recent results of efforts to increase the density in LHD and investigating the density limit from various perspectives during the radiating collapse including the plasma behaviour in the divertor region, the radiation profiles and the relationship between the radiated power, electron density and electron temperature.

2. Peak Density Parameters and Scaling in LHD

LHD is the largest superconducting heliotron-type fusion device with an averaged minor radius of $a = 0.65 \text{ m}$ and a major radius of the plasma axis of 3.6 m [19]. In

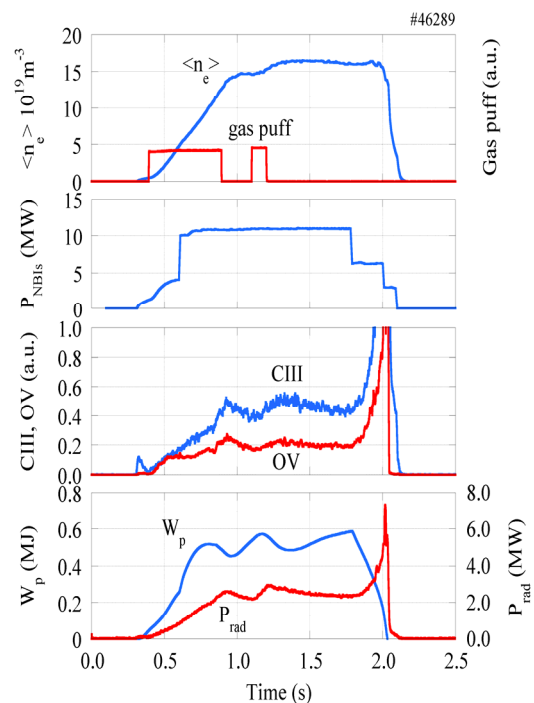


Fig. 1 Typical waveforms of a high density discharge using gas puff fuelling (shot #46289) (a) line-averaged density and gas-puff timing, (b) deposited NBI power, (c) spectroscopy signals from OV and CIII, and (d) total plasma stored energy and total radiated power.

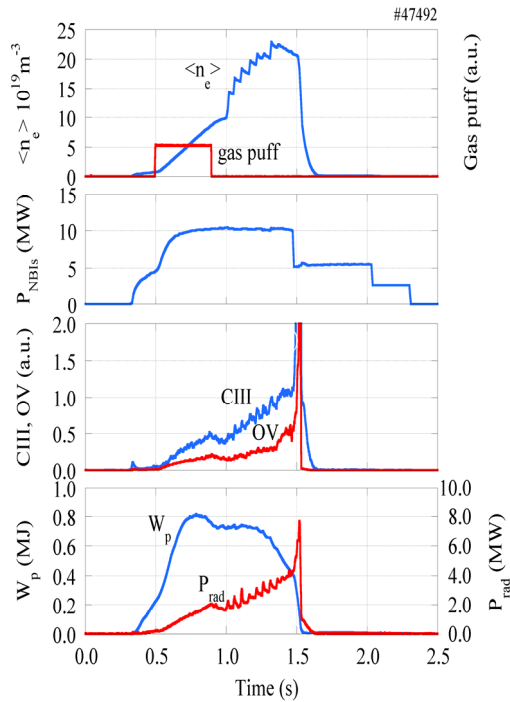


Fig. 2 Typical waveforms of a high density discharge using gas puff and hydrogen pellet fuelling (shot #47492) (a) line-averaged density and gas-puff timing, (b) deposited NBI power, (c) spectroscopy signals from OV and CIII, and (d) total plasma stored energy and total radiated power.

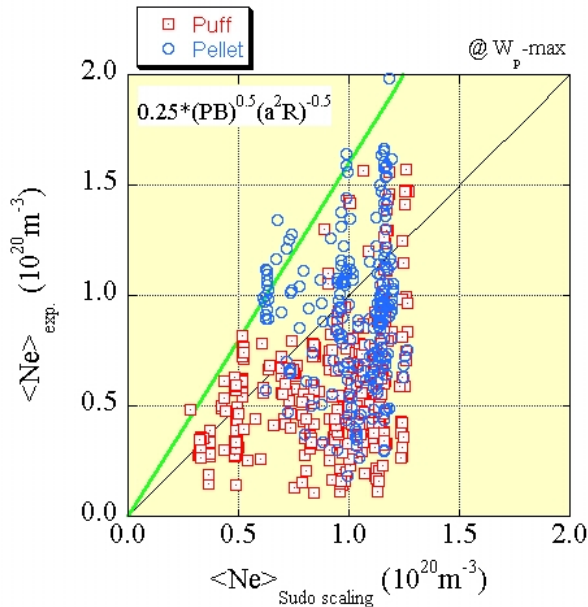


Fig. 3 Density limit scaling for LHD data taken at the timing of maximum stored energy plotted versus the Sudo limit. Red squares indicate gas puff fuelling only and blue circles indicate gas puff and pellet fuelling. Green line indicates a factor of 1.6.

the latest experimental campaign in LHD, line-averaged densities of up to $1.6 \times 10^{20} \text{ m}^{-3}$ have been sustained for more than 0.7 s by 11 MW neutral beam injection using gas puff fuelling. An example of one of these high density discharges is shown in Fig. 1. This value of density corresponds to 1.36 times Sudo scaling, which is close to what was observed previously. In addition, using multiple hydrogen pellets, the density has been increased to over $2 \times 10^{20} \text{ m}^{-3}$ transiently as shown in Fig. 2. Discharges in which the gas puffing or pellet fuelling were increased beyond these levels terminated in a radiating collapse, therefore these discharges represent the operational limits for the density of the LHD plasma during the 2003–2004 campaign for gas puff fuelling and pellet fuelling, respectively. Density data taken at the maximum in the stored energy for gas puff and pellet fueled discharges from the 2003–2004 campaign also shows a limit which exceeds the Sudo limit by a factor of approximately 1.6 (see Fig. 3) as was seen in previous studies [8, 10].

3. Evolution of Parameters Leading to Radiating Collapse at the Density Limit

3.1 Evolution of bulk parameters

The terminal phase of a typical discharge with radiating collapse is shown in Fig. 4. During the steady state portion of the discharge prior to 2 s, the radiation is proportional to the line-averaged density, \bar{n}_e . This proportional relationship is what we would expect from the well known equation giving the radiated power from impurities, P_Z ,

$$P_Z = V n_e n_Z L_Z(T_e) \quad (1)$$

where V is the radiating volume, n_Z is the impurity density, L_Z is the cooling rate for the impurities, which is a function of the electron temperature, T_e , when the other parameters are independent of the electron density, or constant during this phase. This does not mean that these other parameters do not change during this phase, but only that the product $V n_Z L_Z$ is constant during this phase. For instance we know that the electron temperature is dropping during this phase, but the contribution of L_Z to this term may remain constant as the peak radiation zone moves in from the edge towards the core, changing only the location of the peak radiation zone, not its contribution to the total radiation, or it may be compensated by some change in n_Z . During this phase the main radiation is believed to come from outside of $r/a = 0.9$ as indicated by Fig. 10 and most likely from the low temperature ergodic edge region. The light impurity signals OV and CIII normalized to the density also are seen to be relatively constant during this phase, as seen in Fig. 4 (c), indicating that the products of the cooling rate and impurity density for these particular charge states are also constant. This phase ends when the radiative thermal instability is suddenly triggered as indicated by the sharp

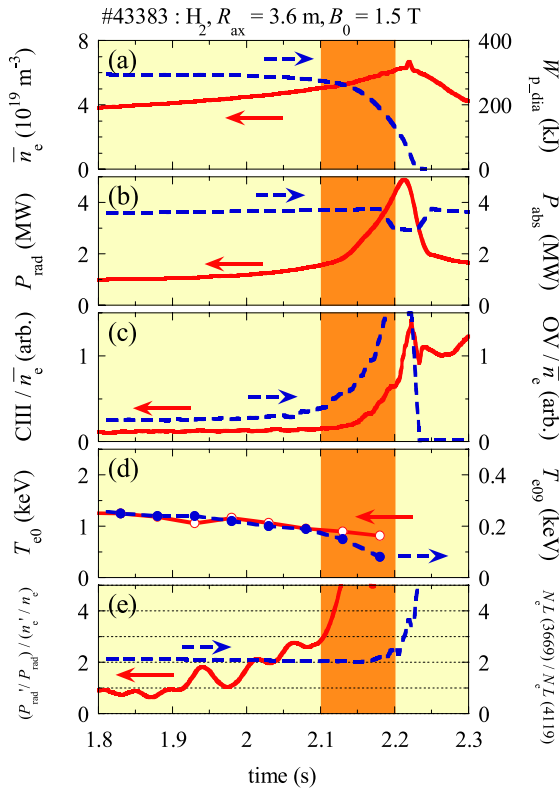


Fig. 4 Typical waveforms of a discharge terminated by radiating collapse in LHD for shot #43383.

increases in P_{rad} and the light impurities emission. The radiative thermal instability is commonly understood as a positive feedback mechanism which results in the range of temperatures where the impurity cooling rate has an inverse dependence on the electron temperature. Therefore as the electron temperature drops due to radiation losses the radiation grows and further cools the plasma. This continues until the input power can no longer sustain the plasma and the plasma collapses. After the sudden onset of the thermal instability the radiation increases rapidly and its dependence on the density becomes stronger than linear (as seen in Fig. 5) as the plasma column starts to contract. This indicates that the other parameters, n_Z and $L_Z(T_e)$ have some dependence on n_e and are contributing to the increase in the radiation. The critical time ($t_c = 2.1$ s in Fig. 4 and Fig. 5) of the onset of the thermal instability is defined as when P_{rad} is proportional to \bar{n}_e^3 (see Fig. 4 (e) and Fig. 5, where $x = (dP_{\text{rad}}/dt/P_{\text{rad}})/(d\bar{n}_e/dt/\bar{n}_e)$, which we call the density exponent given by $P_{\text{rad}} = \bar{n}_e^x$). The density exponent of 3 is somewhat arbitrarily chosen as being well above one. This gives us a convenient means to quantify the onset of the thermal instability for comparing various discharges.

Figure 6 shows the evolution of the electron temperature at $\rho = r/a = 0.9$ versus the line-averaged density. The temperature increases as the plasma is heated and the stored energy increases, then peaks as the stored energy

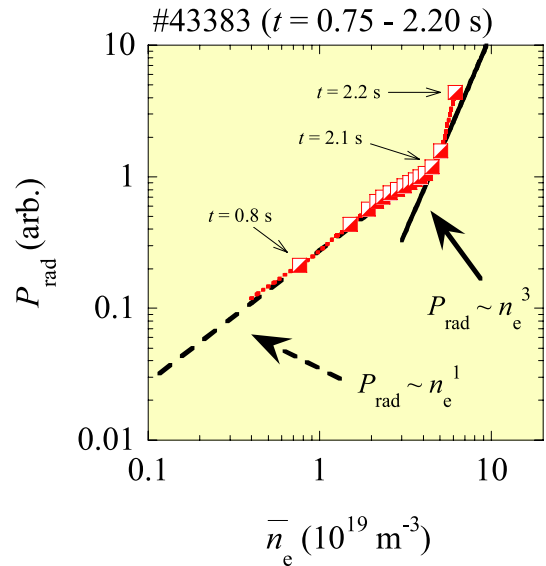


Fig. 5 Radiated power dependence on density for LHD shot #43383.

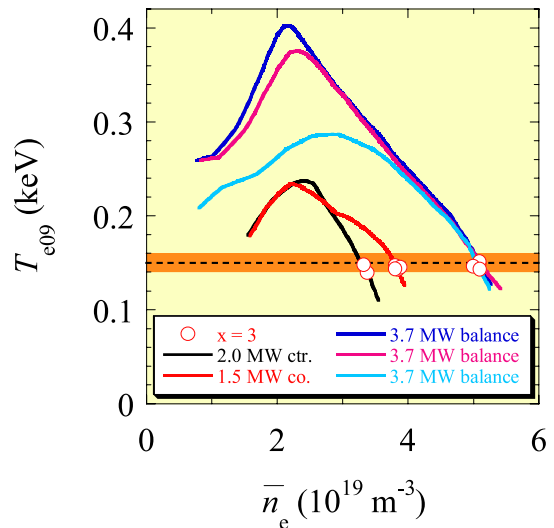


Fig. 6 Evolution of edge electron temperature at $\rho = 0.9$ as a function of line-averaged density for varying input powers.

saturates. In an attempt to maintain constant pressure and stored energy, the temperature then decreases as the density continues to increase with gas puffing. However pressure also decreases as confinement degrades in the high density regime as discussed at the end of Sec. 1 above. As the electron temperature decreases, the cooling rate suddenly increases at some critical temperature depending on the impurity. For carbon this is in the range of 12 eV and for oxygen this is in the range of 40 eV for the average-ion coronal-equilibrium model [20]. However this critical temperature can be shifted up due to non-coronal equilibrium properties resulting from charge exchange recombination and impurity transport as was discussed in a pre-

vious report [10]. The white circles indicate the points in time, t_c , where $x = 3$, which we defined as the onset of the thermal instability. These points occur invariably at a temperature of 150 eV at $\rho = 0.9$. At this time, when the thermal instability is initiated, the edge (at $\rho = 0.9$) temperature is consistently observed to decrease to about 150 eV regardless of the input power and plasma density as is seen in Fig. 6 and regardless of the magnetic axis position, the puffed gas or the density as seen in Fig. 7. This characteristic edge temperature is insensitive to P_{abs} and \bar{n}_e as long as the wall condition is maintained, confirming that the onset of the thermal instability is closely tied to the edge plasma temperature. If the wall condition is degraded by the increase of metallic impurities, then the threshold temperature would be expected to increase leading to an earlier onset of the thermal instability at a lower density limit for the same input power. While we believe the thermal instability is triggered further out in minor radius at a lower electron temperature, we do not have good measurements in that range of electron temperature (below 50 eV), therefore we have chosen $\rho = 0.9$ for our analysis point. After t_c the temperature at $\rho = 1$ has dropped below the measurable limit of 50 eV, which is the temperature below which the oxygen radiation grows, rapidly leading to the onset of the radiative thermal instability as seen in Fig. 4(c). This is followed ~ 50 ms later by CIII which becomes unstable at a lower electron temperature. The radiation is also enhanced after t_c as the hot plasma column shrinks leaving an increasingly larger volume of low temperature plasma in which the light impurities radiate strongly. After t_c the edge temperature decreases faster than that at the core (Fig. 4(d)), presumably due to radiative cooling in the edge by light impurities. Comparison

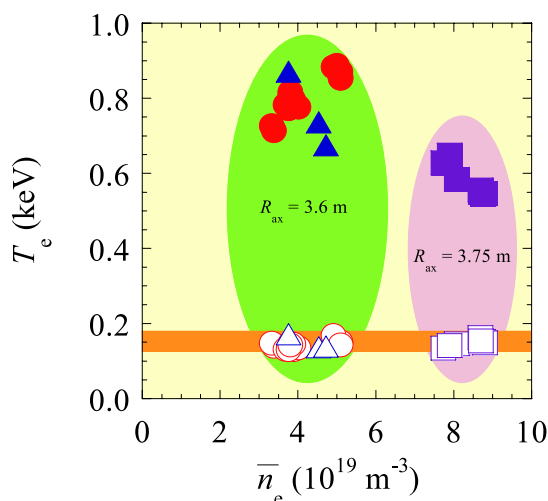


Fig. 7 Edge ($\rho = 0.9$, open symbol) and core ($\rho = 0.1$, solid symbol) electron temperature dependence on line-averaged density for Hydrogen (red) and Helium (blue) puffing and axis positions at the onset of the thermal instability, when $x = 3$.

of the growth rate of the OV radiation in Fig. 4(c) with the decay rate of the stored energy in Fig. 4(a) also indicates that the edge radiative losses are responsible for the confinement degradation.

3.2 Radiated power fraction

Comparison of the input power of the NBI and the radiated power from the bolometer in Fig. 4(b) indicates that the total radiated power fraction is around 40% at the onset of the thermal instability at t_c and then increases rapidly to transiently exceed the input power at the collapse. This level of radiated power fraction is commonly observed at the onset of the thermal instability leading to the radiating collapse as is seen in Fig. 8 in data from the third (2000-2001) and fourth (2001-2002) campaigns of LHD. These are for discharges with hollow radiation profiles or low levels of metallic impurities from the stainless steel walls during discharges using the graphite helical divertor. However, much higher radiated power fractions of up to 100% were observed without collapse in discharges using a stainless steel divertor [21] or a stainless steel limiter [22] with significant levels of radiation from the core resulting from metallic impurities. This indicates that the edge radiation from lighter impurities is playing the primary role in determining the onset of the thermal instability and the collapse of the plasma at the density limit. These results are consistent with the previous observations on ATF [4, 5]. It should be noted that this estimate of the total radiated power in LHD is not based on power balance, but on the volume integration of the radiation profiles for the region inside the last closed flux surface and the ergodic edge region obtained by tomographic inversion of bolometer array signals [23]. Thus, it does not include the divertor leg region

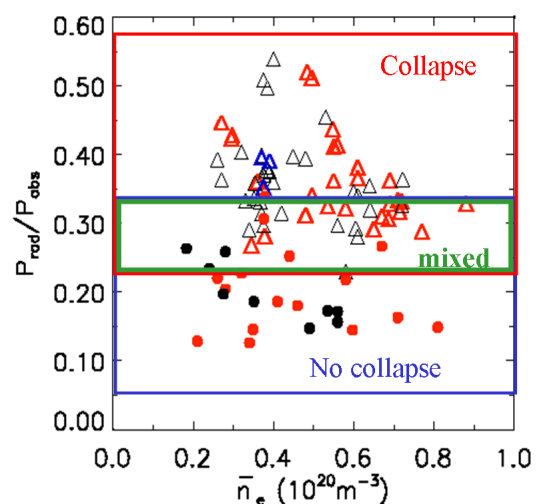


Fig. 8 Radiated power fraction versus density at the onset of the thermal instability for collapsing shots (triangles) and at the peak density for non collapsing shots (circles) from the third and fourth campaigns in LHD.

whose radiation is difficult to estimate due to the limited number of detectors, uncertainty regarding the size of the radiating volume and the toroidal and poloidal asymmetries in this region. Therefore the neglect of this region may result in an underestimation of the total radiated power.

3.3 Edge parameters and role of light impurities

Since the dominant intrinsic light impurities are oxygen and carbon they should be responsible for the strong increase in the radiation from the edge. First we consider the radiation brightness from the divertor, core and edge plasmas in Fig. 9 as the discharge shown in Fig. 4 collapses. One notes that the onset of the thermal instability, as defined by the red dashed line when $x = 3$ for the total radiation, is followed by the development of the previously observed asymmetry in the radiation as the radiation from the inboard channel starts to diverge from the channel located near the outboard edge of the plasma. At the same time the radiation from the divertor leg region is increasing, but not as much as the radiation from the inboard side. The ion-saturation current from the divertor probe begins to drop with the onset of the thermal instability and the radiation asymmetry as it approaches a detached state. Finally, considering the density exponents of the light impurities signals, CIII and OV, and the radiated power, one notes that a thermal instability occurs in the OV as well as in the CIII, but that the CIII signal most closely matches the timing of the total radiated power indicating that carbon is the dominant impurity assuming that the CIII signal is representative of the total radiation from

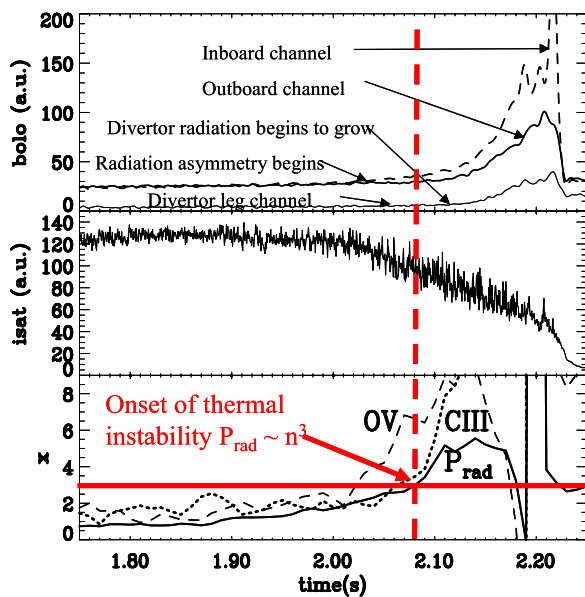


Fig. 9 Time evolution of bolometer intensity, divertor ion saturation current, and the density exponent for the total radiated power, CIII and OV data shown in Fig. 4.

carbon. Since the temperature ranges at which the average coronal equilibrium cooling rates [24] peak are different for carbon (around 6 eV) and oxygen (around 20 eV) and since these are matched by the temperatures at which the ion abundance fractions peak for CIII and OV respectively, one can claim that CIII is representative of carbon and OV for oxygen as far as the comparison of these two impurities is concerned. This temporal progression also makes sense in that OV radiation should peak at a higher temperature (20 eV) than CIII (6 eV), based on the peaks in their abundance fractions, and therefore a thermal instability should occur earlier in the OV as the edge temperature drops. While the temperatures at which these peak values occur should change as the conditions depart from coronal equilibrium during the collapse (recombination dominant), the same general relationships should hold (carbon radiating at a lower temperature than oxygen, etc.). In addition, the above suggestion, that carbon is the dominant impurity (or that oxygen does not significantly contribute to the radiation), is consistent with observations before and after boronization, that while the reduction of OV radiation is stronger than that seen in the reduction of CIII, the reduction in CIII more closely matches the reduction in the total radiated power [12].

3.4 Evolution of radiation profiles during collapse

In Fig. 10 the evolution of the radiated power density profile from a tomographic inversion of the bolometer array data at the horizontally elongated cross-section [23] is shown. In the steady state portion of the discharge the profile is hollow. After the onset of the thermal instability the strongly radiating zone broadens and moves inward minor radially. Similar radiation profile evolutions were observed during the thermal collapse of ATF plasmas [4, 5]. Also

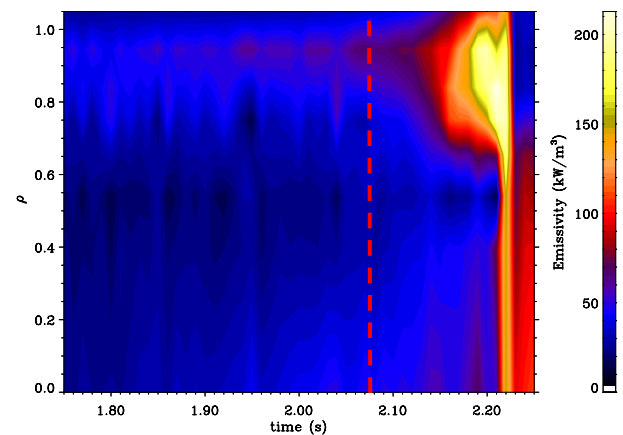


Fig. 10 Evolution of radiated power density profile from a tomographic inversion during the radiating collapse of shot #43383. Red dashed line indicates the onset of the radiative instability ($x = 3$).

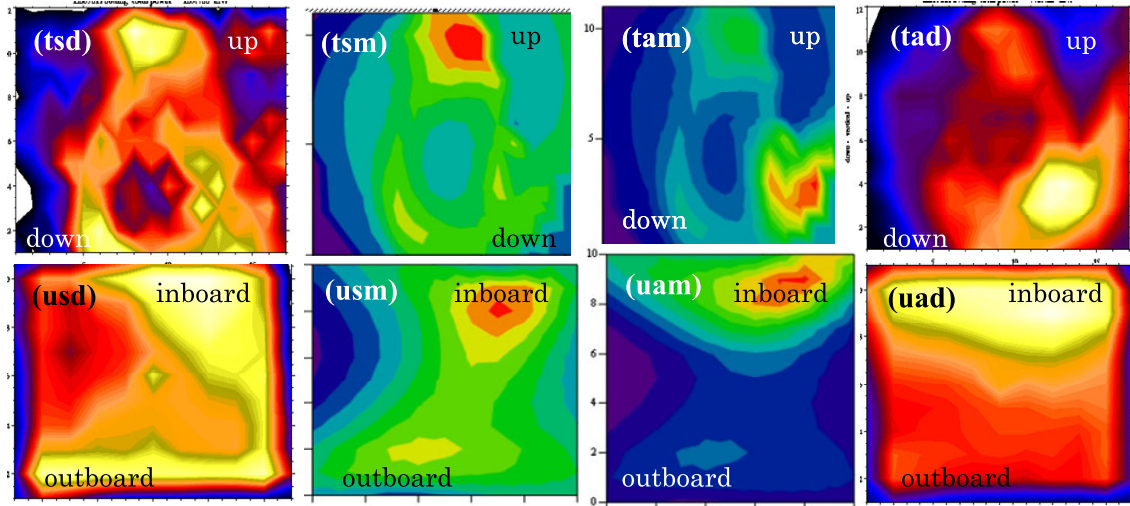


Fig. 11 LHD shot # 28961 IRVB radiation intensity image (d) data (radiation increases with changing color black-blue-purple-red-orange-yellow) from (u) upper and (t) tangential ports during the (s) steady state ($t = 2.0$ s) and (a) asymmetric phases of the discharge ($t = 2.16$ s) compared with reconstructions from (m) model profiles (radiation increases with changing color purple-blue-green-yellow-orange-red).

one notes some indication of growth in the core radiation. At the edge of the plasma one notes the radiation reaches a maximum then decreases, then increases again. This is also seen in the inboard channel of the bolometer in Fig. 9 and may be related to the two peaks observed in the cooling rate of the impurities as a function of electron temperature. One should take care in the quantitative evaluation of the radiation profile during the collapsing phase as the asymmetry in the radiation signal may lead to errors in the tomographic inversion. These errors should be mitigated in this case by the orientation of the array which fans out vertically while the asymmetry has an inboard-outboard nature.

3.5 Radiation asymmetry at collapse

As was seen in Fig. 9 and as was reported previously [8, 10, 11] a MARFE-like asymmetry is observed during the radiating collapse in various diagnostics including two resistive bolometer arrays, Thomson scattering and the FIR interferometer, each located at a different toroidal angle spread through one half of the torus. All of these diagnostics indicate that the low temperature, high density, high radiation region is located on the inboard side, suggesting that this poloidally asymmetric feature is toroidally symmetric. In Fig. 11 we show the results of two imaging bolometers [23] at two different times, compared with images calculated from models of the radiation. The left hand set of images come from the steady state period of the discharge which has a poloidally and toroidally symmetric hollow profile which is confirmed by comparison with the images calculated from a toroidally and poloidally symmetric hollow radiation profile. In the right hand set of images, the data from the imaging bolometers taken from

later in the same discharge during the radiating collapse are compared with images calculated from the same hollow profile, $S(\rho)$, multiplied by a poloidally asymmetric (yet toroidally symmetric) term (a function of the poloidal angle, θ , in degrees) given as

$$S(\rho, \theta) = S(\rho) \cdot [1 + F(\theta)]$$

and

$$F(\theta) = \{[1 + \cos(\theta + 150)]/2\}^{50}.$$

This data shows the high radiation region moving to the inboard side slightly below the midplane as reported earlier [11].

In Fig. 12 the tomographic reconstructions for the same shot and time slices as in Fig. 11 are shown from two arrays of AXUV diodes which are mounted in a semi-tangential cross-section on LHD [23]. This is at a toroidal location which is one third of the way around the machine from the imaging bolometers described earlier. The data shown is from the same discharge and time slices shown in Fig. 11. At the toroidal location of these arrays a gas puff valve is located directly beneath the arrays. The strong signal at the bottom of Fig. 12(a) comes from the puffed-in gas. Besides this feature the radiation is rather symmetric. In Fig. 12(b) the high radiation zone has moved to the inboard side, but at a poloidal angle which is closer to the horizontal midplane than that seen in Fig. 11. The comparison in Fig. 11 of the model with the data taken together with the results from the diodes in Fig. 12 and other diagnostics mentioned above indicates that this phenomenon is roughly toroidally symmetric. That is to say that it does not have a strong dependence on the proximity of the wall which varies considerably with respect to the toroidal and

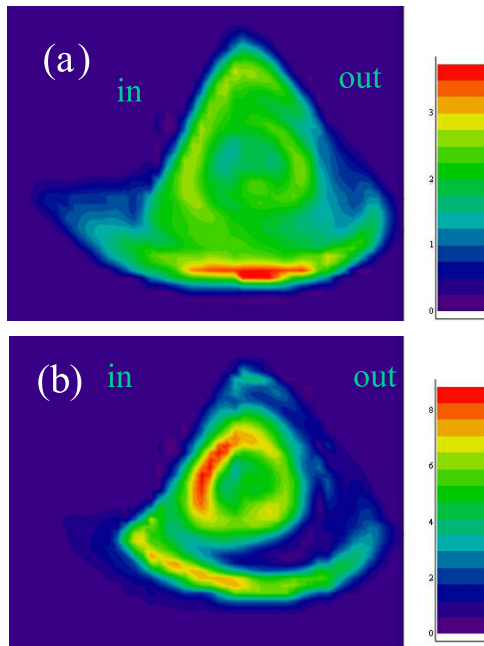


Fig. 12 Two dimensional tomographic images of radiation intensity measured with AXUVD arrays in LHD for the same shot and time slices (a – 2.0 s, b – 2.16 s) shown in Fig. 11.

poloidal angles and it does not have a strong helical dependence tying it to the rotational transform which is close to one at $r/a = 0.9$. If either of these were the case then the data images would look much different than the axisymmetric model. In addition to the low temperature, highly radiating properties of this phenomenon, this axisymmetry is another aspect which it has in common with a MARFE.

4. Discussion

That LHD plasmas can achieve high density steady state discharges at levels which are 1.6 times the Sudo limit has been confirmed with the most recent data taken at NBI powers of up to 11 MW. The assumption that the collapse of the plasma at the density limit is caused by a radiative thermal instability is supported by several observations. (1) There is a threshold edge temperature below which the radiative thermal instability is initiated, leading to the collapse. (2) As the plasma collapses, radiation from OV increases first (since it radiates at a higher temperature) followed by CIII (radiating at a lower temperature) which is thought to be the dominantly radiating intrinsic impurity. (3) Radiation profiles show that as the temperature drops and the plasma collapses, the radiating zone broadens and moves inward. Typically higher densities can be achieved by pellet fuelling than by gas puffing as was seen in Figs. 1 and 2. This is attributed to the core fuelling by pellets which should result in more peaked density profiles and lower edge densities and thus higher edge temperatures compared to the gas puff fuelling. Therefore a higher average density should be achieved before the crit-

ical edge temperature is reached in the case of pellet fuelling compared to gas puff fuelling. Additional evidence that the poloidally asymmetric feature observed during the collapse is roughly toroidally symmetric indicates that this phenomenon is a toroidal effect, as in a tokamak MARFE, and is not related to the geometry of the magnetic field nor of the vacuum vessel, both of which are highly three-dimensional in LHD. Finally, studies show that confinement in the high density regime is degraded compared to ISS95 scaling due to a weakening temperature dependence of the thermal diffusivity [13–16]. This degradation of confinement as density increases leads to an even more rapid drop in the temperature thereby more rapidly reaching the edge threshold temperature where the onset of the radiative thermal instability is triggered.

As was mentioned previously, the position at which the thermal instability begins to grow is not thought to be at $\rho = 0.9$ where we measure a critical temperature of 150 eV, but rather further out and at lower temperature. A likely candidate for this position is the edge of the ergodic region where the long field line region gives way to the short field line divertor region [25]. Since the region outside this point should have a much smaller differential volume, the radiation from that region should not contribute significantly to the cooling of the plasma and the overall power balance. Indeed, we saw in Fig. 9 that the radiation brightness measured from the divertor region is small compared to the channels passing through the core and edge of the plasma. Only as the ergodic region is entered, moving in from the divertor leg, would the radiating volume increase strongly. Therefore the critical point for the onset of the radiative thermal instability is thought to be reached when the electron temperature at the edge of the ergodic region drops below the critical temperature for carbon below which the cooling rate increases significantly. At that point in time and space the combination of the increased cooling rate and the larger radiating volume could result in a rapid increase in the radiation as the temperature continues dropping. However this is difficult to confirm due to the lack of measurements at the x-point.

Another unresolved aspect of this process is the role played by the impurity density. While we have evidence that the radiation from carbon is playing a key role in the radiating collapse, it is not clear if the rapid increase in radiation can be solely attributed to the dropping edge temperature leading to an increase in the cooling rate, or if the impurity density might be increasing due to some enhanced transport or recycling of impurities. Recent measurements of radial electric field during the collapse indicate that transition of the edge electric field from positive to negative due to an increase of the density may be contributing to the inward flux of impurities [26], however direct evidence of an influx of impurities was not seen. During the breathing phenomena, a thermal instability was initiated in the light impurities as the temperature dropped and then recovered as heavy impurities diffused out of the

plasma and the temperature recovered [21]. Modeling of the light impurity radiation during this process indicated that the transport and densities of the light impurities did not change significantly, but that the increase in the light impurity radiation could be attributed solely to the increase in the cooling rate due to drop in the electron temperature and to changes in the electron density [27]. Since the process for the light impurities is thought to be similar in the case of these collapsing plasmas, it is believed that the influx of impurities is not playing a major role in these collapsing plasmas. Further clarification of these issues will require detailed transport modeling of spectroscopic data from during the plasma collapse.

In this paper we show evidence that the density is limited by a critical edge temperature. However the density scaling put forward by Sudo [3] is still thought to be valid as the density at which this critical temperature is reached should depend on the input power, plasma volume and confinement (magnetic field). While the density limit in LHD appears to be well above the scalings seen for other helical devices, this study does not provide a new scaling for LHD. One difficulty in deriving such a scaling is in determining the criteria for the selection of the density to be used in the scaling study. In previous studies the value of the density used was that taken when the stored energy reached a maximum in time. However this does not necessarily represent the maximum attainable density. We would suggest that a future scaling study for LHD use, as a criteria for the selection of the density, the onset of the thermal instability as defined in this paper as the point when the radiation increases as the third power of the density. Experiments on LHD (not reported in this paper) using cessation of gas puffing or addition of NBI power to recover from the collapse after the onset of the thermal instability indicate that the level of density achieved at the onset of the thermal instability may be sustainable using the appropriate feedback mechanism (for instance the inboard/outboard asymmetry observed in the bolometer array brightness signals) to avoid the collapse. Another technique to avoid the collapse and raise the operational density limit might

be to provide additional heating localized in the edge. For instance, using ECRH as was suggested earlier [5].

Acknowledgments

This work was performed with the support of NIFS06ULPP528.

- [1] M. Greenwald, *Plasma Phys. Control. Fusion* **44**, R27 (2002).
- [2] H.C. Howe *et al.*, *Controlled Fusion and Plasma Physics* (Proc. 16th Eur. Conf. Venice, 1989), vol.13B, part II, European Physical Society, Geneva 683 (1989).
- [3] S. Sudo *et al.*, *Nucl. Fusion* **30**, 11 (1990).
- [4] S. Hiroe *et al.*, *Nucl. Fusion* **32**, 1107 (1992).
- [5] M.A. Ochando *et al.*, *Nucl. Fusion* **37**, 225 (1997).
- [6] L. Giannone *et al.*, *Plasma Phys. Control. Fusion* **42**, 603 (2000).
- [7] L. Giannone *et al.*, *Plasma Phys. Control. Fusion* **44**, 2149 (2002).
- [8] B.J. Peterson *et al.*, *Phys. Plasmas* **8**, 3861 (2001).
- [9] L. Giannone *et al.*, *Plasma Phys. Control. Fusion* **45**, 1713 (2003).
- [10] Yuhong, Xu *et al.*, *Nucl. Fusion* **42**, 601 (2002).
- [11] N. Ashikawa *et al.*, *J. Nucl. Mater.* **313-316**, 1103 (2003).
- [12] K. Nishimura *et al.*, *J. Plasma Fusion Res.* **79**, 1216 (2003).
- [13] H. Yamada *et al.*, *Nucl. Fusion* **43**, 749 (2003).
- [14] J. Miyazawa *et al.*, *J. Plasma Fusion Res.* **81**, 302 (2005).
- [15] J. Miyazawa *et al.*, *Plasma Phys. Control. Fusion* **47**, 801 (2005).
- [16] J. Miyazawa *et al.*, *Plasma Phys. Control. Fusion* **48**, 325 (2006).
- [17] U. Stroth *et al.*, *Nucl. Fusion* **36**, 1063 (1996).
- [18] For Example, U. Stroth, *Plasma Phys. Control. Fusion* **40**, 9 (1998).
- [19] O. Motojima *et al.*, *Nucl. Fusion* **45**, S255 (2005).
- [20] D.E. Post *et al.*, *At. Data Nucl. Tables* **20**, 397 (1977).
- [21] B.J. Peterson *et al.*, *Nucl. Fusion* **41**, 519 (2001).
- [22] B.J. Peterson *et al.*, *J. Nucl. Mater.* **313-316**, 1178 (2003).
- [23] B.J. Peterson *et al.*, *Plasma Phys. Control. Fusion* **45**, 1167 (2003).
- [24] D.E. Post *et al.*, *At. Data Nucl. Tables* **20**, 397 (1977).
- [25] T. Morisaki *et al.*, *J. Nucl. Mater.* **313-316**, 548 (2003).
- [26] K. Ida *et al.*, *Nucl. Fusion* **45**, 39 (2005).
- [27] B.J. Peterson *et al.*, *J. Plasma Fusion Res. Series* **3**, 99 (2000).